JACS
JOURNAL OF THE AMERICAN CHEMICAL SOCIETY
pubs.acs.org/JACS
Article

Dynamically Stable Active Sites from Surface Evolution of Perovskite Materials during the Oxygen Evolution Reaction

Pietro P. Lopes,*,‖ Dong Young Chung,‖ Xue Rui,‖ Hong Zheng, Haiying He, Pedro Farinazzo Bergamo Dias Martins, Dusan Strmcnik, Vojislav R. Stamenkovic, Peter Zapol, J. F. Mitchell, Robert F. Klie, and Nenad M. Markovic*

Cite This: J. Am. Chem. Soc. 2021, 143, 2741−2750

Read Online

ACCESS | Metrics & More | Article Recommendations | Supporting Information

ABSTRACT: Perovskite oxides are an important class of oxygen evolution reaction (OER) catalysts in alkaline media, despite the elusive nature of their active sites. Here, we demonstrate that the origin of the OER activity in a $La_{1-x}Sr_xCoO_3$ model perovskite arises from a thin surface layer of Co hydr(oxy)oxide (CoO_xH_y) that interacts with trace-level Fe species present in the electrolyte, creating dynamically stable active sites. Generation of the hydr(oxy)oxide layer is a consequence of a surface evolution process driven by the A-site dissolution and O-vacancy creation. In turn, this imparts a 10-fold improvement in stability against Co dissolution and a 3-fold increase in the activity−stability factor for CoO_xH_y/LSCO when compared to nanoscale Co-hydr(oxy)oxides clusters. Our results suggest new design rules for active and stable perovskite oxide-based OER materials.

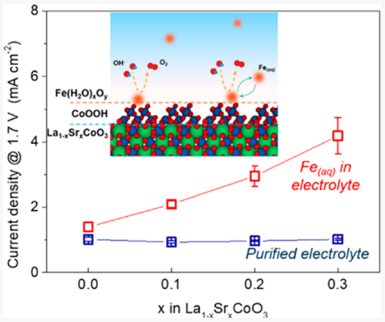

INTRODUCTION

The oxygen evolution reaction (OER) is an integral process of many electrochemical energy conversion and storage systems including H_2 production from water electrolysis,[1−3] metal−air batteries,[4] and fuel production from CO_2 reduction,[5] all essential technologies in a circular economy.[6] Further development to improve the efficiency and lifetime of these devices must rely on advanced materials to drive the OER and, most importantly, that are unhindered by the thermodynamic inverse activity−stability relationships.[7] In acid-based electrolyzer, IrO_x catalyst electrodes have shown the best compromise between O_2 production rates (activity) and metal dissolution rates (stability),[8,9] as described by a high activity−stability factor (ASF).[10] Similarly, insights into the activity−stability relationships of cost-effective and earth-abundant materials have just begun to provide new design rules for advanced alkaline-based electrolyzers.[11]

Two classes of transition metal oxides are most promising to promote OER in alkaline media, 3d transition metal (TM) hydr(oxy)oxides[12−16] and perovskite oxide materials of the form ABO_3[17−23], where A stands for an alkali earth or rare earth cation and B stands for a 3d transition metal cation. While the nature of the active sites in hydr(oxy)oxides still remains elusive, recent findings suggest that Fe impurities from the electrolyte play a major role as a dynamically stable active site.[11] The ability to change compositions of both A- and B-sites in perovskite oxides enables great versatility in tuning their bulk band structure,[17,18] and therefore their reactivity. Changes in the B-site cation, such as Ni, Co, Fe, or Mn, have been correlated to promotion of the direct H_2O/OH^- oxidation mechanism,[17,19] with mixed Co and Fe B-sites displaying the highest OER activity.[19−21] Alternatively, different A-site cations, including La, Sr, or Ba, can reportedly trigger O_2 production via indirect conversion of surface oxygen from the crystal lattice into O_2, while the newly created O-vacancies (O-vac) are replenished by H_2O/OH^-.[22,23]

Despite the apparent success in the correlations between the bulk solid-state band structure and the OER activity trends,[24,25] there remain a number of unanswered questions surrounding the OER catalytic properties of perovskite oxides. First, given that surface reconstruction has been shown to occur during the OER,[20,26−33] it is critical to evaluate the true nature of the surface formed in the course of the reaction. Such surface changes possibly create new active sites that may have unique activity and stability properties (evolved surface), bearing little-to-no relationship to the bulk band structure of the perovskite itself.[34] In addition, the dynamics of the surface reconstruction remain unresolved, with important contributions from atomic-scale dissolution events and the formation of O-vac that must be considered. Lastly, the extent to which trace-level Fe impurities from the electrolyte can impact the perovskite oxide reactivity is still unknown, as those impurities are always present in commercial alkaline solutions.[12,35,36]

Received: August 24, 2020
Published: January 5, 2021

https://dx.doi.org/10.1021/jacs.0c08959
J. Am. Chem. Soc. 2021, 143, 2741−2750

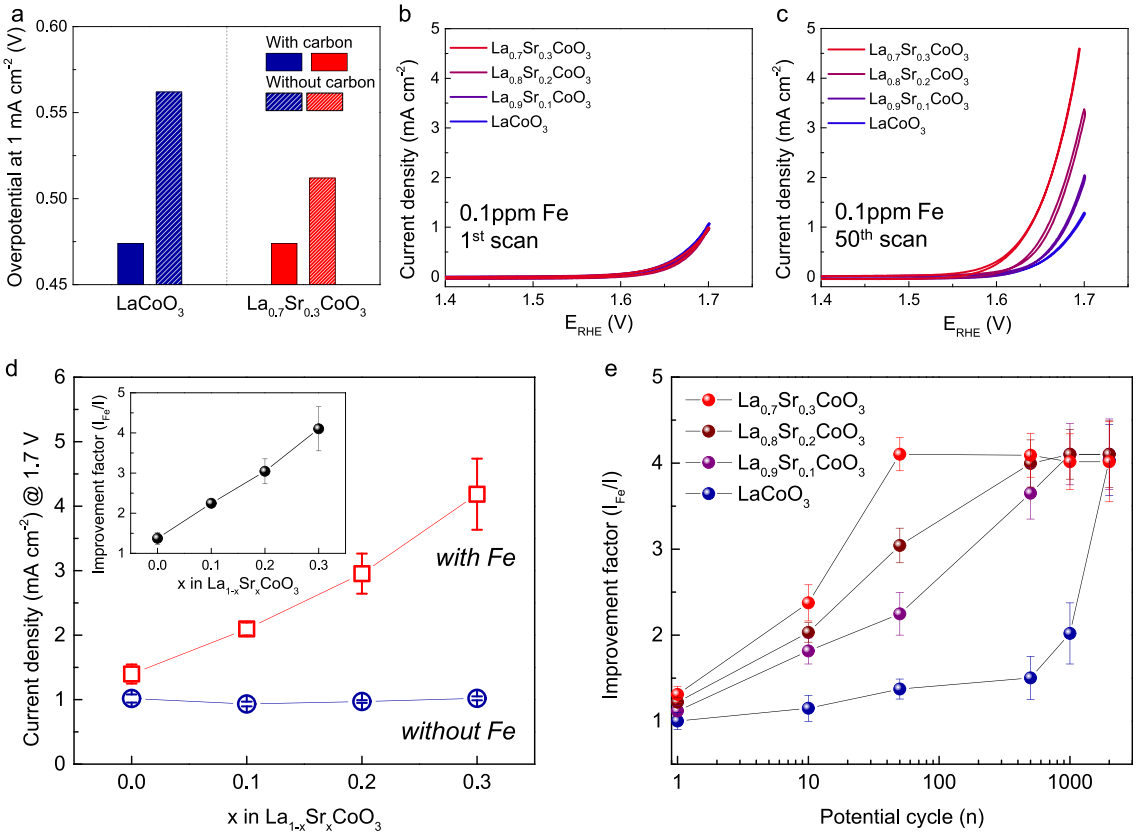

Figure 1. OER activity trends in LSCO-*x* materials under well-defined electrochemical conditions. (a) OER overpotential values measured at 1 mA cm^{-2} from cycling the electrode in highly purified (clean) 0.1 mol L^{-1} KOH at 22 °C for LSCO-0 and LSCO-30 with and without the addition of carbon powder. (b) First OER polarization curve for LSCO-0, 10, 20, and 30% Sr content in A-sites and (c) after 50 potential cycles up to 1.7 V in 0.1 mol L^{-1} KOH deliberately containing 0.1 ppm of Fe$_{(aq)}$. (d) Comparison of OER current density measured at 1.7 V for LSCO-*x* samples precycled 50 times as shown in (c) as a function of the Sr-doping levels in the A-site for electrolytes with and without 0.1 ppm of Fe$_{(aq)}$. Inset shows the O_2 production rate enhancement due to the presence of Fe ($j_{Fe}/j_{no\text{-}Fe}$) as a function of Sr-doping levels. Measurements were taken at least three times, and average values are presented with the standard error bar. (e) Growth of Fe-induced OER enhancement factor as a function of potential cycles for LSCO-0, 10, 20, and 30% Sr-doping levels. Measurements were taken at least three times, and average values are presented with the standard error bar.

Thus, establishing the functional links at the atomic scale between perovskite properties, surface reconstruction dynamics, and electrolyte impurities will provide new insights on how to design active and stable OER electrode materials in alkaline media.

Here, we report a study of stoichiometric single-crystalline Sr-doped $LaCoO_3$ particles, $La_{1-x}Sr_xCoO_3$ (hereafter LSCO-*x*, where *x* indicates Sr atomic concentration), as a model perovskite oxide electrode material for OER in purified alkaline electrolyte. We demonstrate that the origin of the OER activity arises from a few nanometers thick Co hydr(oxy)oxide (CoO_xH_y) layer that interacts with trace-level Fe$_{(aq)}$ in the electrolyte, creating dynamically stable active sites. The formation of the stable hydr(oxy)oxide layer is a consequence of the surface evolution driven by A-site dissolution and O-vac formation, as experimentally confirmed by ex situ identical location scanning transmission electron microscopy (IL-STEM) at atomic resolution, Raman spectroscopy, and in situ inductively coupled plasma−mass spectrometry (ICP-MS). Further, experimental and density functional theory (DFT)-based theoretical analyses reveal a 10-fold gain in stability against Co dissolution and a 3-fold increase in the ASF values for the evolved CoO_xH_y /LSCO surface layer when compared to other CoO_xH_y-based materials. The interaction between Fe species from the electrolyte and 3d transition metal (TM) hydr(oxy)oxide enables the LSCO/CoO_xH_y-Fe electrode/electrolyte interface to be highly active and stable toward O_2 production.

RESULTS AND DISCUSSION

Characterization of LSCO OER Activity in Ultrapure Electrolytes. First, the OER activity trends of stoichiometric single-phase LSCO-*x* (*x* = 0, 10, 20 and 30) single-crystal particles were established in highly purified 0.1 mol L^{-1} KOH (see Materials and Methods section for synthesis, purification protocol, and characterization results shown in Figure S1 in the Supporting Information).[11] The ability to synthesize the LSCO under high O_2 pressure ensures full oxygen stoichiometry (e.g., typical oxygen content assay of 2.993 ± 0.005), creating unique electronic states as well as the ability to explore the role of O-vac independent from the A-site doping level.[37] In addition, the intrinsic differences in electronic conductivity observed at varying Sr-doping levels may mask the true perovskite reactivity,[38−40] particularly for poor electronic conductors, such as LSCO-0. This is exemplified in Figure 1a, as the OER overpotential (η), which denotes the difference between the electrode potential at 1 mA cm$_{geo}^{-2}$ and the thermodynamic OER redox potential of 1.23 V vs RHE, is at least 50 mV higher in LSCO-0 compared to LSCO-30 in

https://dx.doi.org/10.1021/jacs.0c08959
J. Am. Chem. Soc. 2021, 143, 2741−2750

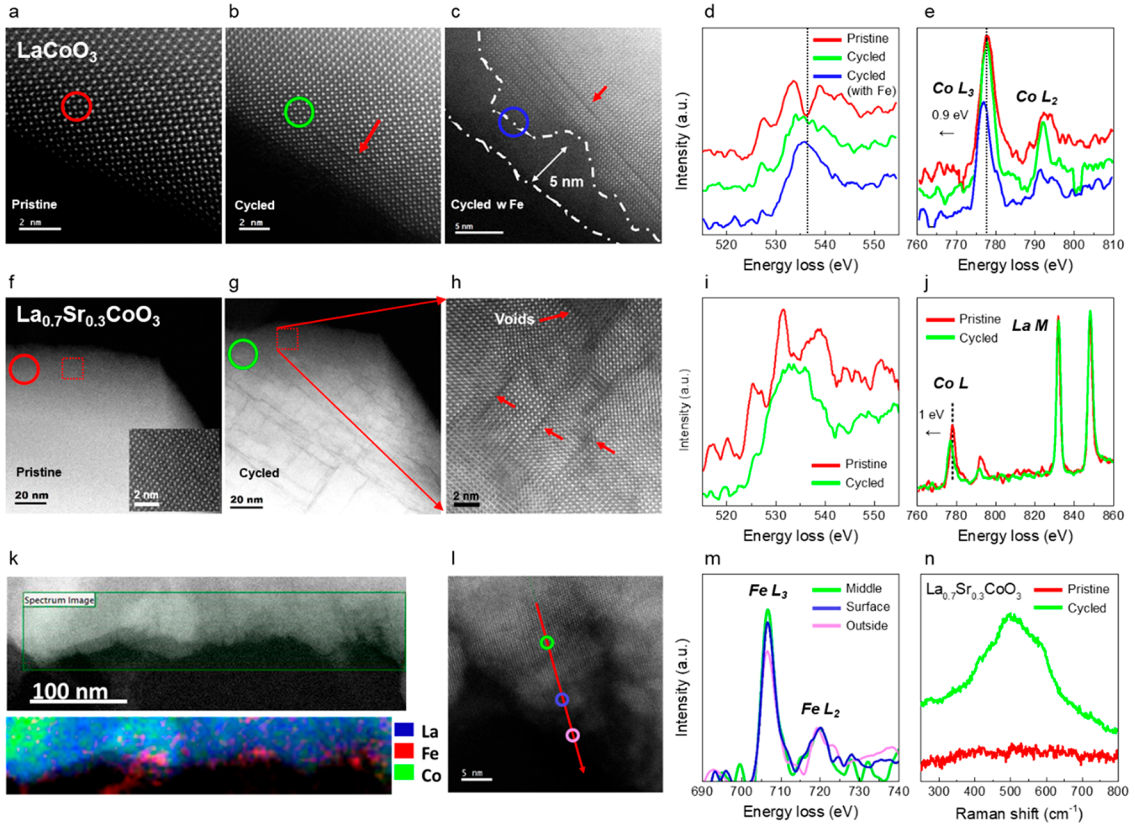

Figure 2. Probing the surface reconstruction as a consequence of potential cycling LSCO surfaces in alkaline media. Identical location STEM images (a) of pristine LSCO-0, (b) after 50 cycles up to 1.7 V in clean 0.1 mol L^{-1} KOH, and (c) after an additional 50 cycles in KOH containing 0.1 ppm of $Fe_{(aq)}$ in the electrolyte. Representative EELS spectra for (d) O K-edge and (e) Co L_2- and L_3-edges for samples shown in (a), (b), and (c). STEM images (f) of pristine LSCO-30 (inset: high magnification showing the lattice fringes indicative of the initial perovskite structure), (g) after 50 cycles up to 1.7 V in clean 0.1 mol L^{-1} KOH, and (h) after an additional 50 cycles in KOH containing 0.1 ppm of $Fe_{(aq)}$ in the electrolyte. Representative EELS spectra as correspondingly marked in panels (a–g) for (i) O K-edge and (j) Co L_2- and L_3-edges for LSCO-30 images shown in (f), (g), and (h). (k) EDS mapping of LSCO-30 surface after the extensive cycling shown in (h), depicting the atomic distribution of La, Co, and Fe over the amorphous surface. (l) High-resolution STEM images (spot indicates where EELS was measured in (m)). Representative EELS spectra in (m) for Fe L_3-edge at different regions of the cycled LSCO-30. (n) Raman spectra of LSCO-30 before and after cycling, indicating formation of CoO_xH_y surface species.

purified KOH. To remove any interference from large intrinsic conductivity differences, we employed a LSCO-x/high surface area carbon electrode composite, noting that, once the limitations of conductivity are removed, there is no OER activity difference beyond experimental error between the LSCO-x samples in purified KOH electrolyte (Figure 1a).

However, there is a striking difference in OER activity after introducing 0.1 ppm of $Fe_{(aq)}$ into purified KOH, particularly after subjecting the electrode to multiple potential cycles. While the first scan response shows identical reactivity across all LSCO samples (Figure 1b), cycling these electrodes over 50 scans up to 1.7 V in the $Fe_{(aq)}$-containing electrolyte reveals a marked activity enhancement for the Sr-doped samples, with increasing activity at higher Sr content (Figure 1c). It is worth noting that the OER activity trends summarized in Figure 1d (LSCO-0 < LSCO-10 < LSCO-20 < LSCO-30) are similar to those in previous reports on the effect of Sr doping on OER activity in LSCO materials.[22,23] To allow direct comparison of the effects of Fe on each LSCO-x sample, we determined the Fe-OER activity enhancement factor, defined by the ratio between the current density measured with and without $Fe_{(aq)}$ in the electrolyte ($j_{Fe}/j_{no\text{-}Fe}$) at 1.7 V. From the inset of Figure 1d, it is clear that activation of Sr-doped samples (LSCO-10, 20, and 30) depends on the synergy between the presence of trace amounts of $Fe_{(aq)}$ in the electrolyte and the extent of Sr doping in the A-site. Extending the number of cycles above 2000 cycles in an electrolyte containing 0.1 ppm of $Fe_{(aq)}$ (Figure 1e) reveals that eventually all LSCO samples become more active, with higher Sr-doped LSCO showing faster activation (higher number of sites) before reaching the maximum OER currents (activated state). It is important to note that extended cycling in purified KOH shows no activity changes for all LSCO-x materials (Figure S2). After activation, the Fe-OER activity enhancement factor reaches a saturation plateau at a value of ~4, similar to what is observed for Fe-CoO_xH_y surfaces.[11]

From the activity trends depicted in Figure 1, there are three important features to highlight. First, the OER activity of all LSCO samples is identical under purified KOH, suggesting that the variations in the bulk band structure for a given Sr-doping play only a minor role on LSCO OER catalysis. Second, important activity differences are observed only when $Fe_{(aq)}$ is present in the electrolyte, albeit at trace levels (0.1 ppm). Third, the activity enhancement increases with cycle/time, faster for higher Sr-doping LSCO, eventually leveling off across all LSCO surfaces. These results point to the existence of a highly dynamic electrode/electrolyte interface, with a possible occurrence of surface evolution (changes in the

https://dx.doi.org/10.1021/jacs.0c08959
J. Am. Chem. Soc. 2021, 143, 2741−2750

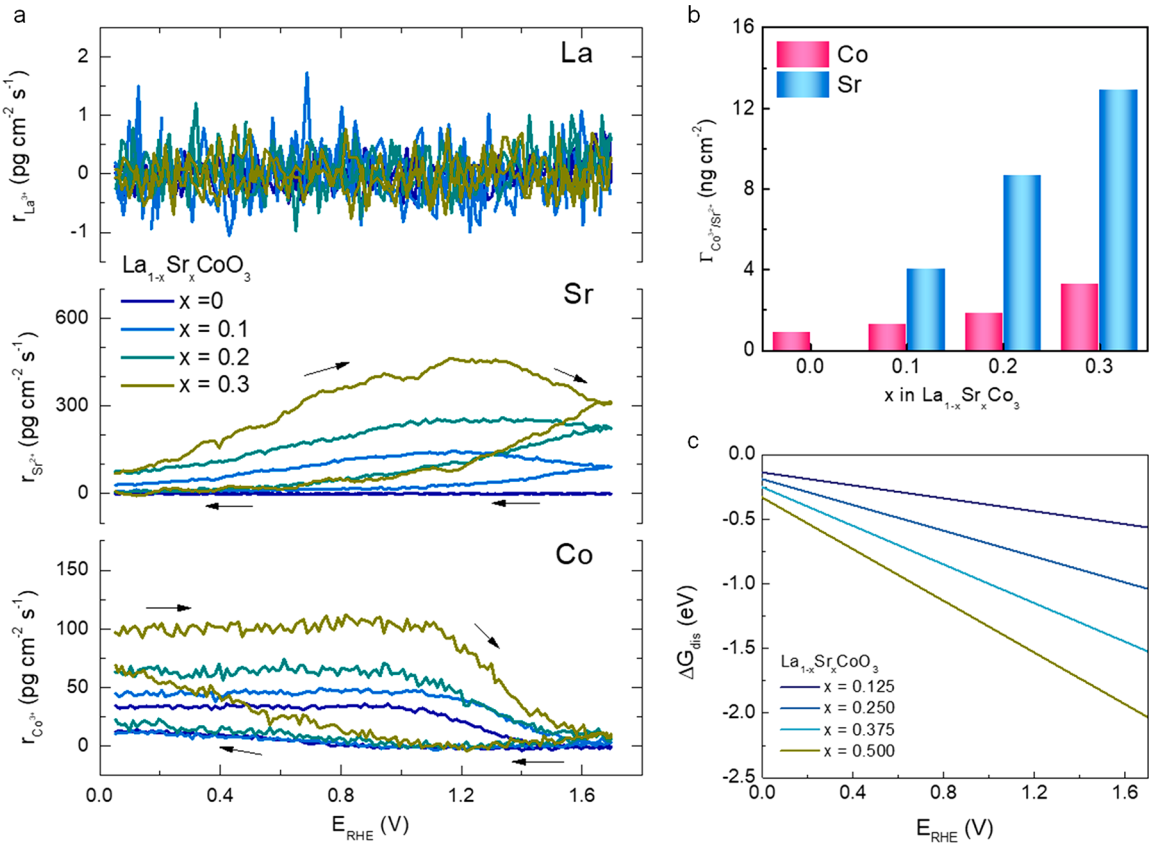

Figure 3. Trends in elemental dissolution rates for LSCO-*x* materials during potential cycling in 0.1 mol L^{-1} KOH. (a) In situ measured La, Sr, and Co dissolution rates as a function of the electrode potential for all four LSCO samples at 0, 10, 20, and 30% Sr-doping level. The arrows indicate the direction of the potential sweep, starting from the positive sweep direction. (b) Total amount of dissolution for Co and Sr after integration of the dissolution profiles depicted in (a). (c) DFT calculated dissolution energy for $La_{1-x}Sr_xCoO_3$ materials as a function of Sr-doping level and increasing electrode potentials.

catalyst surface structure and composition) that takes place during potential cycles, with a direct correlation to the presence of Sr on the A-sites. It is surprising that the observed OER activation is only achieved when $Fe_{(aq)}$ is present in the electrolyte, implying that the changes in the surface sites of the LSCO, or the increase in surface area, are not enough to explain the high OER rates based on the intrinsic LSCO reactivity given by the first scan. However, the observed effect indicates that a dynamically stable active site could be responsible for the OER activity trends as previously observed in 3d TM hydr(oxy)oxides.[11]

Determination of LSCO Surface Evolution Process. To confirm the occurrence of surface evolution, we employed IL-STEM analysis of selected LSCO-0 and LSCO-30 samples. Specifically, we tracked the changes in the surface atomic and electronic structures of the same particles before and after different electrochemical cycling conditions. By analyzing first the pristine materials, then after 50 cycles in purified KOH, and later after an additional 50 cycles in Fe-containing KOH (see experimental details in the Supporting Information), we were able to visualize the occurrence of three key, sequential processes: formation of ordered O-vac, followed by progressive surface amorphization, and finally, localization of Fe species that interact with the newly formed amorphous oxide surface. Figure 2 shows atomic-resolution high-angle annular dark field (HAADF) images acquired using aberration-corrected scanning transmission electron microscopy (STEM) of an LSCO-0 particle in the [001] projection. While imaging the pristine sample (Figure 2a) reveals the expected structure for this perovskite oxide in an area near the particle surface, Figure 2b shows that the same area remains mostly unchanged, except with some slight differences in contrast of a few Co−O layers. As indicated by the red arrows in Figure 2b, some of the Co−O layers appear darker than the rest, suggesting the presence of ordered O-vac after the initial 50 cycles in purified KOH.[41,42] Further potential cycling, now in the presence of Fe as well, reveals that, in fact, there is a progressive disruption of the initial surface morphology as indicated by the broken white lines in Figure 2c (additional contrast on the amorphous region is shown in Figure S3). At the inward surface front, near the crystalline phase, the creation of additional oxygen vacancies is observed as seen by the darker contrast in the Co−O columns and marked by the red arrow.

Further confirmation of the formation of O-vac comes from analyzing the changes in the electronic structure and local chemical composition of the LSCO-0 particle as a function of potential cycling. The electron energy-loss spectra (EELS) of the O K-edge taken from the pristine LSCO-0 particles (Figure 2d) show the expected near-edge fine-structure of the O K-edge for $LaCoO_3$, with the prepeak located at 530 eV, and followed by two main peaks at 534 and 539 eV. The O K-edge prepeak for LSCO-0 is important, as it is directly correlated to the density of empty Co 3d orbitals and, therefore, to the concentration of oxygen vacancies in the sample. While the O K-edge prepeak in LSCO-0 has also been used previously to analyze the Co-ion spin states,[43] our analysis here will focus

https://dx.doi.org/10.1021/jacs.0c08959
J. Am. Chem. Soc. 2021, 143, 2741−2750

only on the effects of oxygen vacancies because their effects on the prepeak intensity are markedly higher than that caused by changes in Co-ion spin state. The extended fine structure also provides information on the long-range order of the crystal, as well as the density of Co 4s and La−O bonding.[43,44] After the initial 50 cycles, the EELS spectra (shown in green) show a clear decrease in the O K-edge prepeak intensity, which indicates an increase in the O-vac content. Additional cycling leads to almost complete suppression of the prepeak transition, and the fine structure of the O K-edge reflects features that are commonly associated with disordered (amorphous) materials. The Co L-edge spectra (shown in Figure 2e) confirm the trend in the formation of oxygen vacancies after cycling, as the Co L_3- and L_2-edge energies shift toward lower energies, indicating a lower Co valence state, in line with a charge-balancing mechanism on the remaining structure.[41,42] Energy-dispersive X-ray spectroscopy (EDS) shows that the Fe concentration in the LSCO-0 particle after the 50 cycles in $Fe_{(aq)}$-KOH is negligible (Figure S4) and cannot account for the changes observed in the EELS spectra shown in Figure 2d and e.

In contrast to the results observed for LSCO-0, the IL-STEM characterization for the LSCO-30 sample shows a much greater surface reconstruction after cycling in clean KOH and subsequently in Fe-containing KOH. Specifically, the pristine sample shows the atomic structure and composition expected for LSCO-30, without any appreciable O-vac content, confirming the success of the synthesis method. However, a high density of ordered oxygen vacancies, as well as voids, is clearly observed near the particle surface after the initial 50 cycles (Figure 2f and h) and after 100 cycles in clean KOH (Figure S5). The O K-edge EELS shows a large decrease in the prepeak intensity after cycling (Figure 2i), as well as a decrease in the Co valence state, indicated by the Co L-edges shifting toward lower energies by 1 eV (Figure 2j). After 50 additional cycles in Fe-containing electrolyte, we find the amorphization of the particle surface, but now with the addition of appreciable amounts of Fe on the particle surface particularly near Co-rich areas (highlighted in red of Figure 2k), and little in the bulk of the particle. Analysis of the Fe L-edge EELS taken from the particle surface, as well the near-surface bulk, suggests that, despite no changes to the L_3-edge peak position, the changes in peak intensity reflect a higher concentration of Fe at the particle surface, without notable variations of the Fe chemical state across the LSCO-30 particle (Figure 2l and m). Further inspection of EDS mapping reveals that the reconstructed surface region is depleted of Sr, with a large presence of lanthanum oxide/hydroxide layer and a Co amorphous layer (Figure 2k), similar to X-ray photoelectron spectroscopy (XPS) findings discussed in Figure S6, while the structure supporting the amorphous film still retains some crystallinity but without Sr (Figures S7 and S8). From the IL-STEM analysis, we confirm that Sr-containing LSCO samples undergo remarkable surface evolution during a relatively short number of potential cycles. Additional surface-enhanced Raman spectroscopy (SERS) analyses before and after 50 potential cycles were performed for both LSCO-0 and LSCO-30 (Figure 2n), confirming that the amorphous surface layer observed from IL-STEM is related to Co-hydr(oxy)oxide species (details in Figure S9).[45,46]

The results shown in Figures 1 and 2 suggest that activation of LSCO surfaces may be related to the formation of O-vac sites, as well as possible preferential A-site dissolution. To unravel the extent of elemental removal in the kinetics of perovskite surface evolution, we measured simultaneously the rates of La, Sr, and Co dissolution using the stationary probe rotating disk electrode method (SPRDE) coupled to an ICP-MS (see details in the Supporting Information),[47] as shown in Figure 3a and b. During one single potential scan experiment, each element present in LSCO shows distinct dissolution profiles that vary in magnitude as a function of the electrode potential. While there is no trace of La dissolution above background levels, Sr begins to dissolve at potentials as early as 0.1−0.2 V. The differences in dissolution observed from La and Sr indicate a selective Sr dissolution from the A-site, and the Sr dissolution rate increases monotonically as a function of the initial Sr-doping level (Figure 3a and 3b). On the other hand, the results on cobalt display a wide dissolution rate plateau at potentials up to 1.2 V that diminishes at higher potentials. This active/passive behavior can be related to the changes in the Co oxidation state (from 2+ to 3+),[48] while the dissolution plateau would be indicative of a limited chemical dissolution step controlled by Co oxidation state and Sr-doping level (Figure 3a). Integration of the elemental dissolution curves in Figure 3a reveals that the total amount of Co dissolution varies from 1 up to 4 ng cm^{-2} at increasing Sr doping, and total Sr loss varies from 4 ng cm^{-2} for LSCO-10 up to 12 ng cm^{-2} for LSCO-30 (Figure 3b). These seemingly small rates of mass loss, on the order of ng cm^{-2}, are consistent with the formation of a few nm thick surface layers after multiple potential cycles (50−100 scans), noting that it is the cumulative effect of consecutive cycling that allows surface evolution to the Co-hydr(oxy)oxide moieties.

Density functional theory (DFT) was used to explore surface evolution kinetics through a thermodynamic model for Sr dissolution that assumes an electrochemical reaction pathway involving oxygen evolution from crystal lattice. In our model, the selective Sr removal gives rise to CoOOH species that appear as a reaction product. Thus, the thermodynamics of Sr dissolution follows the half-reaction

$$\mathrm{La_{1-x}Sr_xCo^{3+\varepsilon}O_3^{-2+\zeta}} + \frac{x}{2}\mathrm{H_2O} = (1-x)\mathrm{LaCoO_3} + x\mathrm{Sr^{2+}} + x\mathrm{CoOOH} + \frac{3}{4}x\mathrm{O_2} + 2x\mathrm{e^-}$$

and the free energies of dissolution as a function of applied potential were calculated as described in Figure S9. Under the assumption of oxygen vacancy formation due to lattice oxygen evolution before the dissolution of Sr, calculated free energies are shown in Figure 3c for $La_{1-x}Sr_xCoO_{3-\delta}$ (x = 0.125, 0.250, 0.375, and 0.500, $\delta = [(x - \varepsilon - 3\zeta)/(2 - \zeta)]$). The Sr dissolution is thermodynamically favorable for all calculated concentrations and becomes more favorable at higher Sr-doping levels (higher x values). The free energy of dissolution also becomes more negative as the electrode potential increases, and, in accordance with Brønsted−Evans−Polanyi principle, corroborates the experimental evidence for faster Sr dissolution in LSCO-x with an increase in applied potential and with higher x values (Figure 3a). Thus, lattice oxygen evolution and formation of oxygen vacancies can contribute to faster A-site dissolution and perovskite conversion to a CoOOH surface layer (Figure S10).

Identification of Active Sites Formed from LSCO Surface Evolution. The rich electrode/electrolyte dynamics that occur at the surface of LSCO perovskites allow the

https://dx.doi.org/10.1021/jacs.0c08959
J. Am. Chem. Soc. 2021, 143, 2741−2750

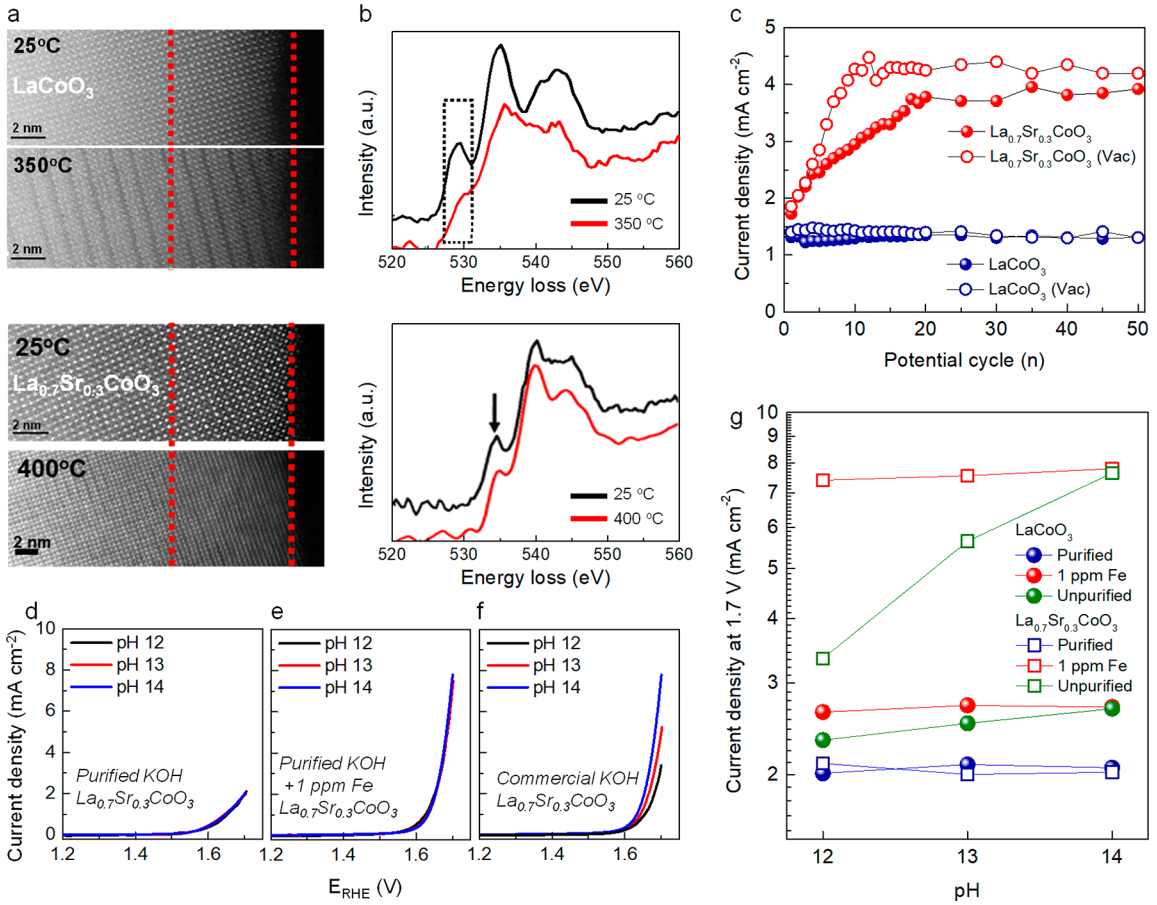

Figure 4. Effect of O-vacancy and pH changes in the OER mechanism on LSCO-*x* samples measured in KOH media. (a) IL-STEM image of LSCO-0 (top) and LSCO-30 (bottom) in the pristine condition and after vacuum annealing at 350 and 400 °C, respectively, for 1 h. (b) Comparison of EELS spectra in the O K-edge for LSCO-0 (top) and LSCO-30 (bottom) showing the creation of extensive O-vac after the vacuum annealing step. (c) Comparison of the effect of induced O-vac due to vacuum annealing on the Fe-OER activity enhancement factor measured in 0.1 mol L^{-1} KOH at 0.1 ppm $Fe_{(aq)}$ as a function of potential cycles in LSCO-0 and LSCO-30. OER polarization curves at pH 12, 13, and 14 measured for LSCO-30 after an initial 50 cycle activation protocol in (d) purified KOH, (e) purified KOH with a deliberate addition of 0.1 ppm of $Fe_{(aq)}$, and (f) KOH solutions at different pH values using unpurified commercial-grade KOH (99.99%). (g) Summary of the individual and combined effects of pH and Fe impurities on the OER current density trends measured at 1.7 V for LSCO-0 and 30% Sr-doping levels.

material to evolve with the formation of hydr(oxy)oxide sites that have a unique interaction with Fe from the electrolyte. The role of trace-level Fe in activating OER can be rationalized in terms of a recently presented dynamically stable active-site model.[11] As Fe hydr(oxy)oxides are the most active but also the most unstable OER active sites in alkaline media,[11] a strong interaction between $Fe_{(aq)}$ and a suitable oxide host, such as 3d TM hydr(oxy)oxides, can allow active Fe species to be dynamically stable at the electrochemical interface. This dynamic stability is established by a dynamic equilibrium between Fe dissolution rate during OER and redeposition rate promoted by $Fe_{(aq)}$ in the electrolyte, while the strong Fe-oxide host interaction retains a large amount of Fe sites at the interface that promote the observed OER rates. Additional DFT results, discussed in detail in Figures S11−S13, indicate a weak interaction between Fe aqueous species and LSCO surfaces with an interaction energy of −0.55 eV, while Fe-CoO_xH_y interaction is much stronger, approximately −1.4 eV, with charge transfer to the underlying CoOOH or LSCO of about $0.13e^-$ to the adsorbed Fe complex according to Bader charge analysis (see Figure S14 for details). This further supports the lack of OER enhancement due to $Fe_{(aq)}$ for all LSCO surfaces in the first potential scan (Figure 1b). The results presented thus far strongly suggest that the OER reactivity observed from LSCO samples does not originate from the perovskite surface itself but rather from CoO_xH_y surface species formed as a consequence LSCO surface evolution, driven by A-site dissolution and O-vac formation. Confirmation of the role of O-vac comes from additional experiments designed to induce O-vac in the LSCO particle after a prestep of thermal annealing in vacuum (see Materials and Methods section in the Supporting Information for additional details). The results depicted in Figure 4a confirm formation of ordered O-vac after vacuum annealing on both LSCO-0(O-vac) and LSCO-30(O-vac). As seen by the dark superlattice features and corroborated by the changes in the O K-edge prepeak intensity and Co L-edges energy shifts measured by EELS (Figure 4b and S15), O-vac are formed without variations in the La, Sr, and Co concentrations. However, neither LSCO-0(O-vac) nor LSCO-30(O-vac) samples displayed any notable differences in their OER activity when measured in purified electrolyte. This corroborates that oxygen vacancies do not directly promote O_2 production on a true perovskite surface (Figure 4c). However, surface evolution and OER activation do occur slightly faster when O-vac are present before electrochemical cycling.

https://dx.doi.org/10.1021/jacs.0c08959
J. Am. Chem. Soc. 2021, 143, 2741−2750

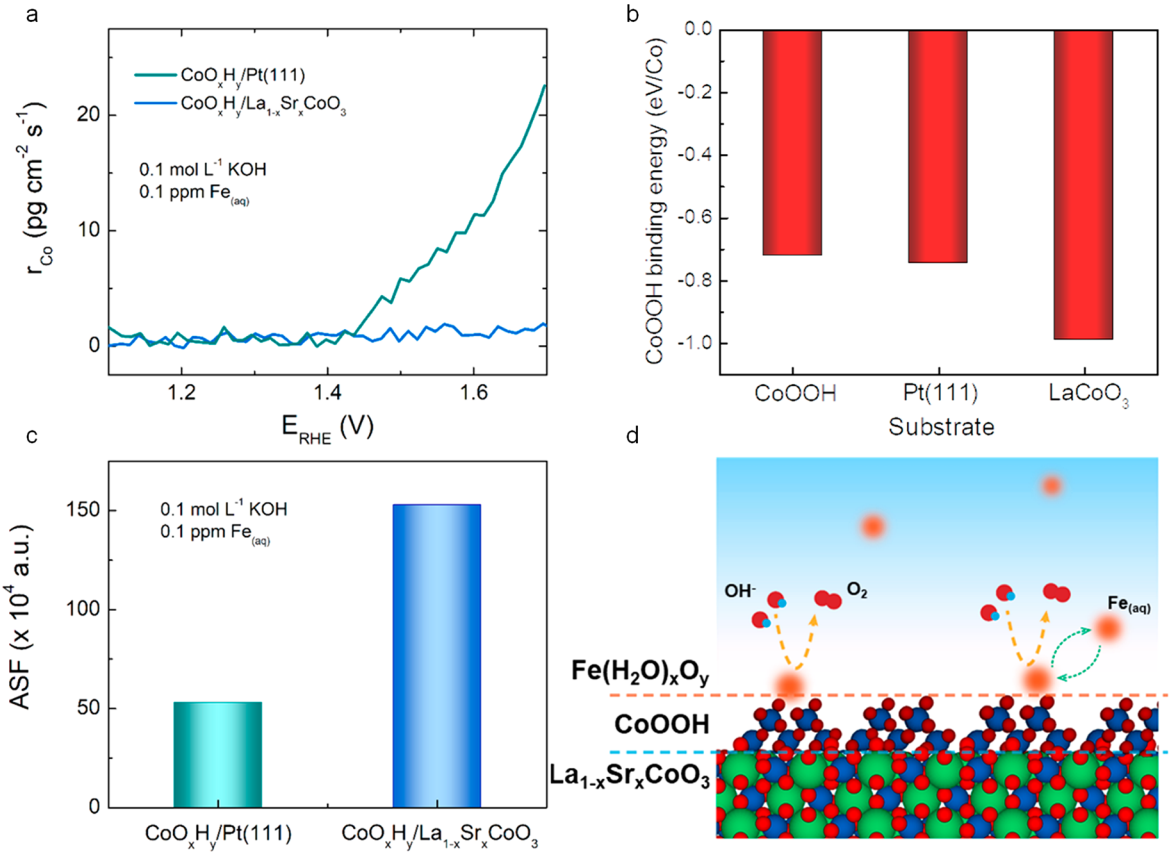

Figure 5. Enhanced stability of CoOOH sites against dissolution during OER from surface evolved LSCO perovskite oxides. (a) In situ Co dissolution rates as a function of electrode potential for LSCO-30 after the initial 50 potential cycles up to 1.7 V and CoO_xH_y cluster deposited over Pt(111) surfaces measured in purified 0.1 mol L^{-1} KOH. (b) DFT calculated CoOOH binding energy to different support structures, corroborating the larger stability against dissolution when CoOOH moieties are present over the LSCO crystal structure. (c) Activity–stability factor (ASF) comparison between CoO_xH_y@LSCO versus CoO_xH_y@Pt(111) in 0.1 mol L^{-1} KOH containing 0.1 ppm $Fe_{(aq)}$ showing an overall 3-fold higher performance for Co hydr(oxy)oxide layer formed from surface evolved LSCO perovskite. (d) Schematic of the multilayered core–shell interface formed over a surface evolved LSCO perovskite oxide, highlighting the Fe active sites that are dynamically stable due to strong interaction with CoOOH surface species.

A key aspect of the reactivity of perovskite is the previously reported occurrence of a nontrivial activity–pH relationship, suggesting the presence of nonconcerted proton–electron transfer steps during indirect OER pathway.[23,49,50] By simply varying the electrolyte pH between 12 and 14 over a (i) highly purified 0.1 mol L^{-1} KOH; (ii) purified KOH with intentional addition of 1 ppm $Fe_{(aq)}$; and (iii) commercial unpurified KOH (see Materials and Methods section in the Supporting Information for additional details), we were able to reconcile the previous activity trends with our dynamically stable active-site model.[23] As depicted in Figures 4d and e and S16, there is no difference in the OER polarization curves for both LSCO-30 and LSCO-0 when the electrolyte is purified or has the same Fe content across all different pH values. However, measuring the OER activity in commercial KOH (Figure 4f) leads to a decrease in the measured activity at lower pH values, a consequence of the 10× and 100× dilution factors in the Fe content for pH 13 and 12, respectively, when compared to pH 14. This effect is particularly strong for the LSCO-30 sample, as its fast surface evolution makes it most sensitive to the variations in the trace Fe content (Figure 1, 2, and 3). The trends in OER current measured at 1.7 V as a function of pH are summarized in Figure 4g, revealing that the origin of the nontrivial activity–pH relationship is a direct consequence of the $Fe_{(aq)}$-CoO_xH_y interaction in uncontrolled electrolyte systems.

An unforeseen benefit of allowing the LSCO surface to evolve to a CoO_xH_y is that it enables interaction with $Fe_{(aq)}$ species, in addition to enhancing by 10-fold the stability against dissolution of CoO_xH_y species at the interface with the LSCO crystal structure. This is shown in Figure 5a, as the dissolution rates at 1.7 V for a CoO_xH_y @LSCO are ca. 1.8 pg cm^{-2} s^{-1}, just slightly above the detection limit, while the Co dissolution rate for CoO_xH_y@Pt(111) is as high as 23 pg cm^{-2} s^{-1}. The stability gain is corroborated by DFT calculations where CoOOH supported over LSCO is almost 0.3 eV more stable than when self-supported or over a Pt(111) surface (Figures 5b and S17). Calculated ASF values for CoO_xH_y@LSCO confirm a 3-fold overall improvement versus CoO_xH_y@Pt(111) surface (Figure 5c), suggesting that the perovskite oxides serve as a strong support for the Fe-interacting oxide hosts. Additional confirmation of the formation of Fe dynamically stable active sites is given by the quick isotopic exchange between ^{57}Fe initially retained at the CoO_xH_y/LSCO surface and ^{56}Fe that was present in the electrolyte (Figure S18). The new reactivity model for perovskite oxides presented here sets a hard limit on the practicality of the O_2 production from lattice oxygen or the validity of the use of a perovskite band structure to predict its catalytic surface properties. In fact, because the occurrences of

https://dx.doi.org/10.1021/jacs.0c08959
J. Am. Chem. Soc. 2021, 143, 2741–2750

Co and Sr dissolution processes were not taken into consideration as important side reactions together with O_2 lattice evolution, the catalytic mechanism for O_2 production from the oxygen lattice sites would only be possible if electrodeposition of the perovskite oxide was a feasible process in alkaline media at potentials where OER takes place. In exchange, our results provide a new set of design rules for active and stable perovskite oxide-based materials ($Fe-BO_xH_y@ABO_3$) for O_2 production. As depicted in Figure 5d, our new model of the electrochemical interface established between a perovskite oxide and the electrolyte involves an electronic conductive ABO_3 core that allows surface evolution and formation of the TM hydr(oxy)oxide shell, where the active $Fe_{(aq)}$ species from the electrolyte can be made dynamically stable to promote O_2 production rates. This multicomponent interface can be manipulated by tuning both A- and B-sites, where changes in the nature and composition of an A-site cation can control the surface reconstruction rates, while changes to B-sites will impact the interaction strength with $Fe_{(aq)}$ species and the stability of the hydr(oxy)oxide layer. We note in passing that changes in the relative stability of the hydr(oxy)oxide layer over the perovskite core structure could depend on epitaxial strain and/or other electronic contributions, an important direction that could be explored on materials that were considered previously unsuitable for OER catalysis.

CONCLUSIONS

In summary, by employing a combination of high-precision synthesis, high-precision electrochemistry, atomic-scale imaging, and theory, we have been able to resolve the nature of active sites in LSCO perovskite oxide-based materials. In turn, it establishes a unified active-site model that can guide the design of perovskite oxide-based materials via the formation of dynamically stable active sites, necessary for active, stable, and cost-effective water electrolysis.

ASSOCIATED CONTENT

Supporting Information

The Supporting Information is available free of charge at https://pubs.acs.org/doi/10.1021/jacs.0c08959.

Experimental procedures (synthesis, characterization, and electrochemical measurement), DFT calculations (method and results), and electrochemical characterization (PDF)

AUTHOR INFORMATION

Corresponding Authors

Pietro P. Lopes − *Materials Science Division, Argonne National Laboratory, Lemont, Illinois 60439, United States;* orcid.org/0000-0003-3211-470X; Email: plopes@anl.gov

Nenad M. Markovic − *Materials Science Division, Argonne National Laboratory, Lemont, Illinois 60439, United States;* Email: nmmarkovic@anl.gov

Authors

Dong Young Chung − *Materials Science Division, Argonne National Laboratory, Lemont, Illinois 60439, United States;* orcid.org/0000-0001-5453-8314

Xue Rui − *Department of Physics, University of Illinois at Chicago, Chicago, Illinois 60607, United States;* orcid.org/0000-0001-7318-5614

Hong Zheng − *Materials Science Division, Argonne National Laboratory, Lemont, Illinois 60439, United States*

Haiying He − *Department of Physics and Astronomy, Valparaiso University, Valparaiso, Indiana 46383, United States*

Pedro Farinazzo Bergamo Dias Martins − *Materials Science Division, Argonne National Laboratory, Lemont, Illinois 60439, United States;* orcid.org/0000-0002-7078-0378

Dusan Strmcnik − *Materials Science Division, Argonne National Laboratory, Lemont, Illinois 60439, United States;* orcid.org/0000-0002-3021-2771

Vojislav R. Stamenkovic − *Materials Science Division, Argonne National Laboratory, Lemont, Illinois 60439, United States;* orcid.org/0000-0002-1149-3563

Peter Zapol − *Materials Science Division, Argonne National Laboratory, Lemont, Illinois 60439, United States;* orcid.org/0000-0003-0570-9169

J. F. Mitchell − *Materials Science Division, Argonne National Laboratory, Lemont, Illinois 60439, United States*

Robert F. Klie − *Department of Physics, University of Illinois at Chicago, Chicago, Illinois 60607, United States;* orcid.org/0000-0003-4773-6667

Complete contact information is available at: https://pubs.acs.org/10.1021/jacs.0c08959

Author Contributions

‖P.P.L., D.Y.C., and X.R. contributed equally.

Notes

The authors declare no competing financial interest.

ACKNOWLEDGMENTS

Material synthesis, structural and electrochemical characterization, and theoretical calculations were conducted at Argonne National Laboratory, a U.S. Department of Energy, Office of Science, laboratory operated by UChicago Argonne, LLC, under Contract no. DE-AC02-06CH11357. We acknowledge the support from the Office of Science, Basic Energy Sciences, Materials Sciences and Engineering Division. H.H. acknowledges the support of the University Research Professorship from Valparaiso University. We acknowledge the computational resources provided by the Center for Nanoscale Materials, an U.S. Department of Energy, Office of Science, user facility. R.F.K. and X.R. performed IL-TEM experiments and acknowledge the support from the National Science Foundation (DMR-1831406). The acquisition at UIC of the JEOL JEM ARM200CF was supported by an MRI-R^2 Grant from the National Science Foundation (DMR-0959470), and the upgraded Gatan Continuum spectrometer was supported by a grant from the NSF (DMR-1626065).

REFERENCES

(1) Stamenkovic, V. R.; Strmcnik, D.; Lopes, P. P.; Markovic, N. M. Energy and fuels from electrochemical interfaces. *Nat. Mater.* **2017**, *16*, 57−69.

(2) Staszak-Jirkovsky, J.; Malliakas, C. D.; Lopes, P. P.; Danilovic, N.; Kota, S. S.; Chang, K.; Genorio, B.; Strmcnik, D.; Stamenkovic, V. R.; Kanatzidis, M. G.; Markovic, N. M. Design of active and stable Co-Mo-S_x chalcogels as pH-universal catalysts for the hydrogen evolution reaction. *Nat. Mater.* **2016**, *15*, 197−203.

(3) Niaz, S.; Manzoor, T.; Pandith, A. H. Hydrogen storage: Materials, methods and perspectives. *Renewable Sustainable Energy Rev.* **2015**, *50*, 457−469.
(4) Gasteiger, H. A.; Markovic, N. M. Just a dream or future reality? *Science* **2009**, *324*, 48−49.
(5) Norskov, J. K.; Christensen, C. H. Toward efficient hydrogen production at surfaces. *Science* **2006**, *312*, 1322−1323.
(6) Stahel, W. R. Circular economy. *Nature* **2016**, *531*, 435−438.
(7) Binninger, T.; Mohamed, R.; Waltar, K.; Fabbri, E.; Levecque, P.; Kotz, R.; Schmidt, T. J. Thermodynamics explanation of the universal correlation between oxygen evolution activity and corrosion of oxide catalysts. *Sci. Rep.* **2015**, *5*, 12167.
(8) Danilovic, N.; Subbaraman, R.; Chang, K.; Chang, S.; Kang, Y. J.; Snyder, J.; Paulikas, A. P.; Strmcnik, D.; Kim, Y.; Myers, D.; Stamenkovic, V. R.; Markovic, N. M. Activity-stability trends for the oxygen evolution reaction on monometallic oxides in acidic environments. *J. Phys. Chem. Lett.* **2014**, *5*, 2474−2478.
(9) Danilovic, N.; Subbaraman, R.; Chang, K. C.; Chang, S. H.; Kang, Y.; Snyder, J.; Paulikas, A. P.; Strmcnik, D.; Kim, Y. T.; Myers, D.; Stamenkovic, V. R.; Markovic, N. M. Using surface segregation to design stable Ru-Ir oxides for the oxygen evolution reaction in acidic environments. *Angew. Chem., Int. Ed.* **2014**, *53*, 14016.
(10) Kim, Y.; Lopes, P. P.; Park, S.; Lee, A.; Lim, J.; Lee, H.; Back, S.; Jung, Y.; Danilovic, N.; Stamenkovic, V. R.; Erlebacher, J.; Snyder, J.; Markovic, N. M. Balancing activity, stability and conductivity of nanoporous core-shell iridium/iridium oxide oxygen evolution catalysts. *Nat. Commun.* **2017**, *8*, 1449.
(11) Chung, D. Y.; Lopes, P. P.; Farinazzo Bergamo Dias Martins, P.; He, H.; Kawaguchi, T.; Zapol, P.; You, H.; Tripkovic, D.; Strmcnik, D.; Zhu, Y.; Seifert, S.; Lee, S.; Stamenkovic, V. R.; Markovic, N. M. Dynamic stability of active sites in metal hydr(oxy)oxide for the oxygen evolution reaction. *Nat. Energy* **2020**, *5*, 222−230.
(12) Trotochaud, L.; Young, S. L.; Ranney, J. K.; Boettcher, S. W. Nickel Iron Oxyhydroxide Oxygen Evolution Electrocatalysts: The Role of Intentional and Incidental Iron Incorporation. *J. Am. Chem. Soc.* **2014**, *136*, 6744−6753.
(13) Roy, C.; Sebok, B.; Scott, S. B.; Fiordaliso, E. M.; Sorensen, J. E.; Bodin, A.; Trimarco, D. B.; Damsgaard, C. D.; Vesborg, P. C. K.; Hansen, O.; Stephens, I. E. L.; Kibsgaard, J.; Chorkendorff, I. Impact of nanoparticle size and lattice oxygen on water oxidation on $NiFeO_xH_y$. *Nat. Catal.* **2018**, *1*, 820−829.
(14) Zhang, B.; Zheng, X.; Voznyy, O.; Comin, R.; Bajdich, M.; Garcia-Melchor, M.; Han, L.; Xu, J.; Liu, M.; Zheng, L.; Garcia de Arquer, F. P.; Dinh, C. T.; Fan, F.; Yuan, M.; Yassitepe, E.; Chen, N.; Regier, T.; Liu, P.; Li, Y.; De Luna, P.; Janmohamed, A.; Xin, H. L.; Yang, H.; Vojvodic, A.; Sargent, E. H. Homogeneously dispersed multimetal oxygen-evolving catalysts. *Science* **2016**, *352*, 333−337.
(15) Huang, Z.; Song, J.; Du, Y.; Xi, S.; Dou, S.; Nsanzimana, J. M. V.; Wang, C.; Xu, Z. J.; Wang, X. Chemical and structural origin of lattice oxygen oxidation in Co-Zn oxyhydroxide oxygen evolution electrocatalysts. *Nat. Energy* **2019**, *4*, 329−338.
(16) Dionigi, F.; Strasser, P. NiFe-Based (Oxy)hydroxide Catalysts for Oxygen Evolution Reaction in Non-Acidic Electrolytes. *Adv. Energy Mater.* **2016**, *6*, 1600621.
(17) Bockris, J. O.; Otagawa, T. The Electrocatalysis of Oxygen Evolution on Perovskites. *J. Electrochem. Soc.* **1984**, *131*, 290−302.
(18) Matsumoto, Y.; Yamada, S.; Nishida, T.; Sato, E. Oxygen Evolution on $La_{1-x}Sr_xFe_{1-y}Co_yO_3$ Series Oxides. *J. Electrochem. Soc.* **1980**, *127*, 2360−2364.
(19) Suntivich, J.; May, K. J.; Gasteiger, H. A.; Goodenough, J. B.; Shao-Horn, Y. A Perovskite Oxide Optimized for Oxygen Evolution Catalysis from Molecular Orbital Principles. *Science* **2011**, *334*, 1383−1385.
(20) May, K. J.; Carlton, C. E.; Stoerzinger, K. A.; Risch, M.; Suntivich, J.; Lee, Y.; Grimaud, A.; Shao-Horn, Y. Influence of Oxygen Evolution during Water Oxidation on the Surface of Perovskite Oxide Catalysts. *J. Phys. Chem. Lett.* **2012**, *3*, 3264−370.
(21) Kim, B.; Cheng, X.; Abbott, D. F.; Fabbri, E.; Bozza, F.; Graule, T.; Castelli, I. E.; Wiles, L.; Danilovic, N.; Ayers, K. E.; Marzari, N.; Schmidt, T. J. Highly Active Nanoperovskite Catalysts for Oxygen Evolution Reaction: Insights into Activity and Stability of $Ba_{0.5}Sr_{0.5}Co_{0.8}Fe_{0.2}O_{2+\delta}$ and $PrBaCo_2O_{5+\delta}$. *Adv. Funct. Mater.* **2018**, *28*, 1804355.
(22) Mefford, J. T.; Rong, X.; Abakumov, A. M.; Hardin, W. G.; Dai, S.; Kolpak, A. M.; Johnston, K. P.; Stevenson, K. J. Water electrolysis on $La_{1-x}Sr_xCoO_{3-\delta}$ perovskite electrocatalysts. *Nat. Commun.* **2016**, *7*, 11053.
(23) Grimaud, A.; Diaz-Morales, O.; Han, B.; Hong, W. T.; Lee, Y.; Giordano, L.; Stoerzinger, K. A.; Koper, M. T. M.; Shao-Horn, Y. Activating lattice oxygen redox reactions in metal oxides to catalyze oxygen evolution. *Nat. Chem.* **2017**, *9*, 457−465.
(24) Hwang, J.; Rao, R. R.; Giordano, L.; Katayama, Y.; Yu, Y.; Shao-Horn, Y. Perovskites in catalysis and electrocatalysis. *Science* **2017**, *358*, 751−756.
(25) Song, J.; Wei, C.; Huang, Z.; Liu, C.; Zeng, L.; Wang, X.; Xu, Z. J. A review on fundamentals for designing oxygen evolution electrocatalysts. *Chem. Soc. Rev.* **2020**, *49*, 2196−2214.
(26) Grimaud, A.; May, K. J.; Carlton, C. E.; Lee, Y.; Risch, M.; Hong, W. T.; Zhou, J.; Shao-Horn, Y. Double perovskites as a family of highly active catalysts for oxygen evolution in alkaline solution. *Nat. Commun.* **2013**, *4*, 2439.
(27) Yang, C.; Batuk, M.; Jacquet, Q.; Rousse, G.; Yin, W.; Zhang, L.; Hadermann, J.; Abakumov, A. M.; Cibin, G.; Chadwick, A.; Tarascon, J.; Grimaud, A. Revealing pH-Dependent Activities and Surface Instabilities for Ni-Based Electrocatalysts during the Oxygen Evolution Reaction. *ACS Energy Lett.* **2018**, *3*, 2884−2890.
(28) Yagi, S.; Yamada, I.; Tsukasaki, H.; Seno, A.; Murakami, M.; Fujii, H.; Chen, H.; Umezawa, N.; Abe, H.; Nishiyama, N.; Mori, S. Covalency-reinforced oxygen evolution reaction catalyst. *Nat. Commun.* **2015**, *6*, 8249.
(29) Han, B.; Stoerzinger, K. A.; Tileli, V.; Gamalski, A. D.; Stach, E. A.; Shao-Horn, Y. Nanoscale structural oscillations in perovskite oxides induced by oxygen evolution. *Nat. Mater.* **2017**, *16*, 121−126.
(30) Fabbri, E.; Nachtegaal, M.; Binninger, T.; Cheng, X.; Kim, B.; Durst, J.; Bozza, F.; Graule, T.; Schaublin, R.; Wiles, L.; Pertoso, M.; Danilovic, N.; Ayers, K. E.; Schmidt, T. J. Dynamic surface self-reconstruction is the key of highly active perovskite nano-electrocatalysts for water splitting. *Nat. Mater.* **2017**, *16*, 925−932.
(31) Tong, Y.; Wu, J.; Chen, P.; Liu, H.; Chu, W.; Wu, C.; Xie, Y. Vibronic Superexchange in Double Perovskite Electrocatalyst for Efficient Electrocatalytic Oxygen Evolution. *J. Am. Chem. Soc.* **2018**, *140*, 11165−11169.
(32) Wu, T.; Sun, S.; Song, J.; Xi, S.; Du, Y.; Chen, B.; Sasangka, W. A.; Liao, H.; Gan, C. L.; Scherer, G. G.; Zeng, L.; Wang, H.; Li, H.; Grimaud, A.; Xu, Z. J. Iron-Facilitated dynamic active-site generation on spinel $CoAl_2O_4$ with self-termination of surface reconstruction for water oxidation. *Nat. Catal.* **2019**, *2*, 763−772.
(33) Duan, Y.; Sun, S.; Sun, Y.; Xi, S.; Chi, X.; Zhang, Q.; Ren, X.; Wang, J.; Ong, S. J. H.; Du, Y.; Gu, L.; Grimaud, A.; Xu, Z. J. Mastering Surface Reconstruction of Metastable Spinel Oxides for Better Water Oxidation. *Adv. Mater.* **2019**, *31*, 1807898.
(34) Zhang, R.; Pearce, P. E.; Duan, Y.; Dubouis, N.; Marchandier, T.; Grimaud, A. Importance of Water Structure and Catalysts-Electrolyte Interface on the Design of Water Splitting Catalysts. *Chem. Mater.* **2019**, *31*, 8248−8259.
(35) Corrigan, D. A. The Catalysis of the Oxygen Evolution Reaction by Iron Impurities in Thin Film Nickel Oxide Electrodes. *J. Electrochem. Soc.* **1987**, *134*, 377−384.
(36) Subbaraman, R.; Danilovic, N.; Lopes, P. P.; Tripkovic, D.; Strmcnik, D.; Stamenkovic, V. R.; Markovic, N. M. Origin of anomalous activities for electrocatalysts in alkaline electrolytes. *J. Phys. Chem. C* **2012**, *116*, 22231−22237.
(37) Medling, S.; Lee, Y.; Zheng, H.; Mitchell, J. F.; Freeland, J. W.; Harmon, B. N.; Bridges, F. Evolution of magnetic oxygen states in Sr-doped $LaCoO_3$. *Phys. Rev. Lett.* **2012**, *109*, 157204.

https://dx.doi.org/10.1021/jacs.0c08959
J. Am. Chem. Soc. 2021, 143, 2741−2750

(38) Suntivich, J.; Gasteiger, H. A.; Yabuuchi, N.; Shao-Horn, Y. Electrocatalytic Measurement Methodology of Oxide Catalysts Using a Thin-Film Rotating Disk Electrode. *J. Electrochem. Soc.* **2010**, *157*, B1263−B1268.
(39) Cheng, X.; Fabbri, E.; Nachtegaal, M.; Castelli, I. E.; El Kazzi, M.; Haumont, R.; Marzari, N.; Schmidt, T. J. Oxygen Evolution Reaction on $La_{1-x}Sr_xCoO_3$ Perovskites: A Combined Experimental and Theoretical Study of Their Structural, Electronic and Electrochemical Properties. *Chem. Mater.* **2015**, *27*, 7662−7672.
(40) Petrov, A. N.; Kononchuk, O. F.; Andreev, A. V.; Cherepanov, V. A.; Kofstad, P. Crystal structure, electrical and magnetic properties of $La_{1-x}Sr_xCo_{3-y}$. *Solid State Ionics* **1995**, *80*, 189−199.
(41) Ito, Y.; Klie, R. F.; Browning, N. D.; Mazanec, T. J. Atomic Resolution Analysis of the Defect Chemistry and Microdomain Structure of Brownmillerite-Type Strontium Cobaltite. *J. Am. Ceram. Soc.* **2002**, *85*, 969−976.
(42) Klie, R. F.; Ito, Y.; Stemmer, S.; Browning, N. D. Observation of oxygen vacancy ordering and segregation in Perovskite oxides. *Ultramicroscopy* **2001**, *86*, 289−302.
(43) Klie, R. F.; Zheng, J. C.; Zhu, Y.; Varela, M.; Wu, J.; Leighton, C. Direct Measurement of the Low-Temperature Spin-State Transition in $LaCoO_3$. *Phys. Rev. Lett.* **2007**, *99*, 047203.
(44) Biskup, N.; Salafranca, J.; Mehta, V.; Oxley, M. P.; Suzuki, Y.; Pennycook, S. J.; Pantelides, S. T.; Varela, M. Insulating Ferromagnetic $LaCoO_{3-\delta}$ Films: A Phase Induced by Ordering of Oxygen Vacancies. *Phys. Rev. Lett.* **2014**, *112*, 087202.
(45) Yang, J.; Liu, H.; Martens, W. N.; Frost, R. L. Synthesis and Characterization of Cobalt Hydroxide, Cobalt Oxyhydroxide, and Cobalt Oxide Nanodiscs. *J. Phys. Chem. C* **2010**, *114*, 111−119.
(46) Yeo, B. S.; Bell, A. T. Enhanced Activity of Gold-Supported Cobalt Oxide for the Electrochemical Evolution of Oxygen. *J. Am. Chem. Soc.* **2011**, *133*, 5587−5593.
(47) Lopes, P. P.; Strmcnik, D.; Tripkovic, D.; Connell, J. G.; Stamenkovic, V. R.; Markovic, N. M. Relationships between Atomic Level Surfaces Structure and Stability/Activity of Platinum Surface Atoms in Aqueous Environments. *ACS Catal.* **2016**, *6*, 2536−2544.
(48) Pourbaix, M. *Atlas of electrochemical equilibria in aqueous solutions*; Pergamon Press: Oxford, 1966.
(49) Koper, M. T. M. Theory of multiple proton-electron transfer reactions and its implications for electrocatalysis. *Chem. Sci.* **2013**, *4*, 2710−2723.
(50) Giordano, L.; Han, B.; Risch, M.; Hong, W. T.; Rao, R. R.; Stoerzinger, K. A.; Shao-Horn, Y. pH dependence of OER activity of oxides: Current and future perspectives. *Catal. Today* **2016**, *262*, 2−10.

https://dx.doi.org/10.1021/jacs.0c08959
J. Am. Chem. Soc. 2021, 143, 2741−2750